1   **A RAMAN SPECTROSCOPY STUDY OF STEEL CORROSION PRODUCTS**

2   **IN ACTIVATED FLY ASH MORTAR CONTAINING CHLORIDES**

3

4   M. Criado,[1*] S. Martínez-Ramirez,[2] J. M. Bastidas[3]

5   [1] Instituto de Ciencia de Materiales de Madrid, CSIC, Sor Juana Inés de la Cruz 3,

6   28049 Cantoblanco−Madrid, Spain

7   [2] Instituto de Estructura de la Materia, CSIC, Serrano 123, 28006 Madrid, Spain

8   [3] Centro Nacional de Investigaciones Metalúrgicas, CSIC, Avda. Gregorio del Amo 8,

9   28040 Madrid, Spain

10

11   **Abstract**

12   Raman spectroscopy was used to characterise the corrosion products of

13   reinforcing steel embedded in activated fly ash mortars in the presence of 0.4 and 2%

14   chlorides. Two alkaline solutions with different soluble silica contents were utilised to

15   activate the fly ash. Raman spectra were obtained using two excitation wavelengths

16   (532 and 633 nm) and making power scans to select the suitable conditions of register

17   for each wavelength. The main steel corrosion products identified were iron

18   oxyhydroxides with low crystallinity, goethite (α-FeOOH) and lepidocrocite (γ-

19   FeOOH). These products need to be studied using a spectrometer with the laser line of

20   532 nm at low powers from 0.025 to 0.25 mW or a spectrometer with the laser line of

21   633 nm at high power between 2.5 and 25 mW.

22   **Keywords:** Raman spectroscopy; Alkali activation; Fly ash; Iron corrosion products;

23   Chloride

24   * Corresponding Author, Tel.: +34 91 334 9000; Fax: +34 91 3720623; E-mail Address:

25   mcriado@icmm.csic.es (M. Criado)

26   **Introduction**

27   The degradation of reinforcing steel due to corrosion is of great concern for the

28   durability of concrete structures and can lead to serious economic implications [1−3].

29   The most important causes of reinforcing steel corrosion initiation are the ingress of

30   chloride ions and carbon dioxide to the steel surface. The depassivation of steel rebars

31   can lead to the localised formation of porous oxide layers at the steel/concrete interface.

32   The volume of iron oxide layers is two to four times larger than that of iron, and the

33   high tensile stresses generated by the expansive volume of the corrosion products [4−6]

34   can result in internal microcraking and spalling of the concrete cover. The rate of

35   corrosion is a limiting factor of the remaining service life of a corroding reinforced

36   concrete structure (RCS).

37   Therefore, the study and characterization of corrosion products in reinforced

38   concrete is an important issue with a view to assessing the corrosion state within RCS

39   and predicting their remaining service life. Several techniques like Raman spectroscopy

40   [7], X-ray photoelectron spectroscopy (XPS) [8], Mössbauer spectroscopy [9],

41   ellipsometry [10], secondary ion mass spectrometry (SIMS) [11], and atomic force

42   microscopy [12] have been employed to study the passive film on the steel surface.

43   Micro-Raman spectroscopy is a preferred method because it is a non-destructive

44   technique that is well suited for the in situ characterization of various oxides and

45   oxyhydroxides involved in the corrosion of iron. Moreover this spectroscopy presents

46   two important advantages: the lack of any need for sample preparation and the quick

47   and easy obtainment of water/metal interface spectra [13−16].

48   Iron oxides and oxyhydroxides are known to be sensitive to thermal

49   transformations even at low laser power because they are opaque to visible light and

50   heat up. Indeed, a temperature rise induces a transformation to the most stable phase,

51 i.e. hematite (α-Fe$_2$O$_3$) [15]. As some iron oxides are highly sensitive to laser

52 irradiation, several authors have used a set of density filters to modulate the laser power

53 and avoid any thermal effect on iron (III) compounds [15,17−19].

54 De Faria et al. [20] employed Raman microscopy to investigate the laser power

55 dependence of the Raman spectra of oxides and oxyhydroxides like hematite (α-Fe$_2$O$_3$),

56 magnetite (Fe$_3$O$_4$), wüstite (FeO), maghemite (γ-Fe$_2$O$_3$), goethite (α-FeOOH),

57 lepidocrocite (γ-FeOOH) and feroxyhyte (δ-FeOOH). The results obtained showed that

58 increasing the laser power causes the characteristic bands of hematite to show up in the

59 spectra of most of the studied compounds, with the consequent band broadening and

60 shifts of the hematite spectrum. Under high laser power all the investigated

61 oxyhydroxides showed the characteristic peaks of hematite, with the power threshold

62 being dependent on the surface morphology.

63 Nieuwoudt et al. [21] demonstrated that significant enhancements of the Raman

64 spectra for iron oxides and oxyhydroxides can be achieved using an optimised

65 excitation wavelength of 636.4 nm, providing further improvement over those attained

66 with the 632.8 nm excitation wavelength under similar conditions. When compared, the

67 Raman spectra for standard iron compounds in the low wave number region (<1000

68 cm^{-1}) obtained using a tuneable dye laser with the 636.4 nm line are more intense and

69 well-defined that those obtained using an excitation wavelength of 514.5 nm.

70 Taking into account all these premises, the main aim of this paper was to study

71 the corrosion products formed on steel embedded in alkali activated fly ash (AAFA)

72 mortars in the presence of chloride ions using a Micro-Raman spectrometer with two

73 excitation wavelengths (532 and 633 nm) and making power scans to select the suitable

74 conditions of register for each laser line. Since several oxyhydroxides can be formed as

75 corrosion product it is important to discern if they become from laser irradiation

76 transformation or as corrosion products.

77   The choice of AAFA as cementitious matrix is due to the fact that this is being

78 used in concrete for reasons related with environmental impact, economic sustainability

79 and social responsibility [22]. The alkali activation of type F fly ash consists of mixing

80 the fly ash with highly alkaline solutions (pH>13) and subsequently curing the resulting

81 paste at a certain temperature to produce a solid material. Considering that RCS safety

82 and durability are two of the most important requirements for building protection, the

83 capacity of an AAFA mortar to passivate steel rebars is a necessary property to

84 guarantee both aspects of RCS constructed using these new materials.

85 **Experimental**

86   Concrete reinforcement electrodes were cut from carbon steel plates with a

87 chemical composition of 0.45% C, 0.22% Si, 0.72% Mn, <0.010% P, 0.022% S, 0.13%

88 Cr, 0.13% Ni, 0.18% Cu, and balance Fe. The specimen surfaces were polished with

89 emery paper from 120 to 600, washed with double distilled water and degreased with

90 acetone.

91   The cementitious material used was a type F fly ash (FA) from a coal-fired

92 power plant at Aboño, Asturias, Spain. The chemical composition of the FA is shown in

93 Table 1. The percentage of reactive silica (SiO_2) in the FA, determined according to

94 UNE 80−225−93 standard [23], is 41.23% and the vitreous phase content is 65.60%.

95 The procedure used to determine the vitreous phase content was similar to that

96 described elsewhere [24]. Briefly, 1 g of FA was added to 100 ml of 1% hydrofluoric

97 acid (HF) in a plastic beaker and stirred for 6 h at room temperature. The granulometry

98 distribution, determined by laser ray diffraction, showed only one mode in which

99 approximately 85% of particles were smaller than 45 μm and 50% smaller than 13 μm.

100   The FA was activated using two different highly alkaline solutions with roughly

101   the same sodium oxide (Na_2O) content ($\sim$20%) and varying proportions of soluble SiO_2.

102   The products used to prepare the solutions were laboratory grade reagents: sodium

103   hydroxide (NaOH) pellets and waterglass (Na_2SiO_3) containing 27% SiO_2, 8.2% NaOH,

104   and 64.8% H_2O. One activating solution was prepared with 8M NaOH, and the other

105   with 85% 10M NaOH and 15% waterglass.

106   Accordingly, two types of AAFA mortars were manufactured: one using the

107   NaOH solution (FAA mortar) and the other using the 85% NaOH and 15% waterglass

108   mixture (FAB mortar) with a "liquid/solid" ratio of 0.45. The mortars were prepared

109   with sand/AAFA ratio of 2:1. The moulds containing the fresh AAFA mortars were

110   cured in an oven at 85 ℃ in a saturated water vapour atmosphere for 20 h. Different

111   amounts of sodium chloride (NaCl) (99% pure Panreac PRS−CODEX): 0.4 and 2%

112   chloride (in relation to binder weight) were added to the FA. Two prismatic mortar

113   specimens of each type, with dimensions 8 cm×5.5 cm×2 cm, were prepared for

114   comparative purposes [25]. All the specimens were stored at room temperature in an

115   atmosphere of high relative humidity (RH), $\sim$95%, for up to 720 days.

116   The steel was extracted from the FAA and FAB mortars and Raman spectra

117   were obtained directly from the steel plate surface and analysed. Dispersive Raman

118   spectra at 633 and 532 nm were recorded in a RM 1000 Renishaw Raman Microscope

119   System. The Raman spectrometer is equipped with a Leica microscope and an

120   electrically refrigerated CCD camera. The spectra were obtained with ×50

121   magnification objective lenses. The final spectra were the result of 10 accumulations to

122   improve the signal-to-noise ratio and the integration time was 10 s. The software

123   employed for data acquisition and analysis was Wire for Windows and Galactic

124   Industries GRAMS/32TM. Five scans were recorded to improve the signal-to-noise

125 ratio. The Raman shift was calibrated before the measurements according to the silicon

126 peak at 520 cm^{-1}. The 633 nm line had a laser power from 0.25 to 25 mW and finally,

127 the 532 nm line had a laser power from 0.0005 to 5 mW. The measurements were done

128 directly in the sample (in situ), the sample preparation is not necessary.

129 **Results and Discussion**

130 Fig. 1 shows the steel specimens after extraction from the FA mortars in the

131 presence and absence of chlorides for 720 days of experimentation. The steel specimens

132 embedded in the mortars without chlorides present tiny amounts of corrosion products

133 on a practically smooth surface, indicating that the steel was in the passive state in this

134 new cementitious system. The steel specimens extracted from the chloride-polluted

135 mortars present small fragments of the mortars on their surface and in some regions

136 corrosion product layers are also observed. The amount of corrosion products formed

137 was higher in the presence of 2% chlorides and the steel surface was fully coated in both

138 FAA and FAB mortars.

139 The Raman spectra of iron oxides/hydroxides can be divided into two regions

140 [26]: (i) 1200 to 600 cm^{-1} for both Fe−O−H bending and Fe−O stretching vibration

141 regions; and (ii) 600 to 200 cm^{-1}, this region includes absorptions overlapping of lattice

142 vibrations as well as molecular frequencies. Fe−O stretching vibrations can also be

143 absorbed below 400 cm^{-1}.

144 Fig. 2 shows Raman spectra of a corroded bar embedded in FAA mortar with

145 0.4% chlorides using an optimised excitation wavelength of 532 nm under different

146 laser output powers. In the light regions, no compound was detected in the spectrum

147 obtained with the laser power of 0.0005 mW, perhaps due to the use of a very low laser

148 intensity. In the spectra recorded with 0.025 and 0.05 mW, two broad peaks around 695

149 (the most intense) and 1357 cm^{-1} were detected. These peaks were also observed for the

150   laser powers of 0.25 and 0.5 mW, along with other new peaks at 347, 541 and 1589

151   cm^{-1}. These bands are very broad, indicating the formation of corrosion products of low

152   crystallinity, specifically iron oxyhydroxides [17,18]. Finally, when higher laser powers

153   (2.5 and 5 mW) were employed, several sharp peaks typical of hematite were detected

154   at 210 and 273 (very intense), 380, 478, 579 and 1274 cm^{-1}. The peak positions of this

155   compound do not coincide exactly with those observed in other Raman spectra studies

156   of iron corrosion products [13,18,19,21,27]. These differences may be due to the

157   formation of "modified hematite", which presents a structure with few changes or

158   defects. The formation of modified hematite at 2.5 and 5 mW instead of the iron

159   oxyhydroxides formed at a lower laser power may be due to the transformation of the

160   corrosion phases under the higher laser heat during the measurements [5,20]. The

161   spectrum for the steel embedded in FAA mortar with 0.4% chlorides obtained with a

162   laser power of 5 mW also showed fluorescence, leading to an increase of the Raman

163   intensity, (Fig. 2).

164   In the dark deposits on the steel surface, a power of 0.025 mW detected a series

165   of well-defined peaks at 244, 300, 396 (the most intense), 476, 555, 682, 998, 1116 and

166   1309 cm^{-1}, indicating the presence of goethite [13,18,21,27]. This phase was

167   transformed into modified hematite when the laser power was increased (2.5 mW),

168   similarly to what happened in the light regions.

169   Fig. 3 shows Raman spectra for reinforcing steel embedded in FAA mortars with

170   0.4% chlorides using an optimised excitation wavelength of 633 nm under different

171   laser output powers. In this case, the use of a lower energy laser (6.33 nm) with the

172   powers of 0.25 and 2.5 mW allowed the detection of small peaks whose attribution was

173   complicated. Therefore, these spectra were different to those obtained in the same

174   conditions with the 532 nm laser (Fig. 2), where iron oxyhydroxides and hematite were

175   observed, respectively. Moreover, in the spectra recorded with laser powers between

176   6.25 and 25 mW, typical peaks of iron oxyhydroxides were detected which did not

177   experience changes with the increase in laser power and where the phenomenon of

178   fluorescence did not take place. In another area of the sample, goethite peaks were

179   observed for all the range of powers. This phase was stable under a laser heat of 633

180   nm.

181   Fig. 4 shows Raman spectra of the corroded bar embedded in FAA mortar with

182   2% chlorides using an optimised excitation wavelength of 532 nm under different laser

183   output powers. The spectrum obtained with the laser power of 0.0005 mW did not show

184   peaks for iron compounds. On increasing the laser power (from 0.025 to 0.5 mW) a

185   series of peaks typical of goethite were observed. The height and width of the peaks in

186   the spectrum were higher and sharper respectively when the laser powers were raised

187   (0.25 and 0.5 mW), and therefore the identification of goethite was easier. Major

188   differences were observed in the spectra recorded for the steel embedded in FAA mortar

189   with 2% chlorides at 2.5 and 5 mW, which presented several well-defined peaks

190   detected at 215 and 276 (the most intense), 386, 484, 585 and 1296 cm^{-1} (Fig. 4),

191   indicating the presence of hematite. The positions of these peaks were shifted,

192   suggesting the formation of a modified hematite as occurred in the FAA mortars with

193   0.4% chlorides (Fig. 2). For 5 mW laser power the spectrum showed fluorescence and

194   the peaks assigned to modified hematite lost intensity and definition.

195   Fig. 5 shows Raman spectra for the steel embedded in FAA mortars with 2%

196   chlorides using an optimised excitation wavelength of 633 nm under different laser

197   output powers. Iron corrosion products were not detectable in the spectrum recorded at

198   0.25 mW, but the formation of goethite was detected in the same spectrum with 532 nm

199   the laser line. In this latter case, the presence of goethite was observed in the rest of the

200   spectra with laser powers between 2.5–25 mW. This longer wavelength (633 nm) did

201   not lead to transformation of the compounds under laser heat (position of peaks

202   remained fixed) or produce fluorescence during the measurements.

203   Fig. 6 shows Raman spectra of the corroded bar embedded in FAB mortar with

204   0.4% chlorides using an optimised excitation wavelength of 532 nm under different

205   laser output powers. No peak was observed in the spectrum with the lowest power

206   (0.0005 mW), but for laser powers of 0.025 and 0.05 mW two broads bands (1367 and

207   706 cm^{-1}) corresponding to iron oxyhydroxides were detected. In the spectra obtained at

208   0.25 and 0.5 mW, peaks were also observed at 1603, 523, 374 and 243 cm^{-1} (see Fig.

209   6). The peaks at 1603, 1367, 706, 523 and 374 cm^{-1} were assigned to oxyhydroxides

210   with low crystallinity while the peak at 243 cm^{-1} was allocated to lepidocrocite

211   [13,17,18]. The other lepidocrocite peaks at 1306, 523 and 374 cm^{-1} overlapped with

212   the oxyhydroxides peaks. The intensity of these peaks increased with the power.

213   However, at the laser powers of 2.5 and 5 mW these peaks disappeared and other peaks

214   were located in the positions corresponding to hematite and modified hematite,

215   respectively.

216   Fig. 7 shows Raman spectra for steel embedded in FAB mortars with 0.4%

217   chlorides using an optimised excitation wavelength of 633 nm under different laser

218   output powers. A series of peaks typical of lepidocrocite were detected for all the laser

219   powers employed, but the power of 0.25 mW yielded only small peaks whose

220   attribution was complicated. In the same sample lepidocrocite could not be detected as a

221   single phase using the wavelength of 532 nm. The intensity of the lepidocrocite peaks

222   increased with the power, but their position remained fixed, indicating that this laser

223   line did not cause the transformation of lepidocrocite due to a heating effect as occurred

224   in Fig. 6.

225   Fig. 8 shows Raman spectra for the corroded bar embedded in FAB mortar with

226   2% chlorides using an optimised excitation wavelength of 532 nm under different laser

227   output powers. The spectra acquired with the laser powers of 0.0005 and 0.025 mW

228   were similar that those obtained in the previous steel embedded in FAB mortar with

229   0.4% chlorides. Goethite was distinguished at 0.05 and 0.25 mW, showing peaks at

230   1313, 1122, 991, 689, 544, 479, 396 (the most intense), 300 and 247 cm^{-1}, whose

231   intensity increased with the laser power. In the spectrum recorded using 0.5 mW new

232   peaks were detected at 1313, 670, 400, 291 and 221 cm^{-1}, typical of hematite iron

233   compound. In this phase the transformation of an iron compound to hematite occurred

234   at a lower power (0.5 mW) than in the other samples. The positions of hematite Raman

235   peaks were shifted to lower wavenumbers for higher powers (2.5 and 5 mW), indicating

236   the presence of modified hematite. The spectrum obtained with 5 mW showed

237   fluorescence and the resolution of hematite peaks was very low.

238   Fig. 9 shows Raman spectra for steel embedded in FAB mortars with 2%

239   chlorides using an optimised excitation wavelength of 633 nm under different laser

240   output powers. Small peaks were visible in the spectrum with 0.25 mW for the light

241   regions on the steel surface, see Fig. 9(a). The intensity of these peaks increased with

242   the laser power. The spectra presented peaks at 1306, 1063, 1001, 685, 646, 540, 527,

243   473, 384, 345, 300, 250, 215 and 168 cm^{-1}. Identification of lepidocrocite was clear, by

244   the very narrow and intense 250 cm^{-1} peak. This iron compound presented other peaks

245   at 1306, 646, 527, 384, 345, 300, 215 and 168 cm^{-1}. The peak at 384 cm^{-1} in the Raman

246   spectrum was very intense, confirming the presence of another compound. This new

247   phase was goethite with several peaks at 1306, 1063, 1001, 685, 540, 473, 384 (the most

248   intense), 300, 250 and 215 cm^{-1}. Two iron compounds were detected for a wavelength

249   of 633 nm while only goethite was observed for a wavelength of 532 nm.

250   At 0.25 mW small undefined peaks were observed in the spectrum of the dark

251   regions on the steel surface, see Fig. 9(b). By increasing the laser power (from 2.5 to 25

252   mW) the peaks corresponding to goethite were intensified and clearly identified.

253   The spectra for the light and dark regions obtained with a lower laser energy

254   (633 nm) did not present fluorescence and the iron compounds formed (goethite and

255   lepidocrocite) were stable under laser heat.

256   In order to identify and locate the phases of the corrosion layers on the rebar,

257   including those poorly crystallised, investigations with Raman micro-spectroscopy have

258   been carried out in recent years. In such work the authors have always controlled the

259   laser power, because some iron oxides are very sensitive to laser exposure. Bouchar et

260   al. [28] used density filters to control the laser power on a sample under 100 µW.

261   Moreover, Singh et al. [29] observed that the Raman spectrum presented significant

262   noise when a laser power of less than 1.5 mW was used. El Mendili et al. [30]

263   investigated the stability of the γ-Fe_2O_3 nanoparticles under laser irradiation with laser

264   powers from 0.08 to 48 mW on the sample and thermal treatment (300-1400ºC). At 15

265   mW and 350ºC the vibration modes of maghemite had vanished and low intensity bands

266   attributed to the hematite phase appear in the Raman spectra. These vibration modes

267   became stronger with increase of the laser power and the thermal treatment. Thus the

268   laser power is a very important parameter when making measurements and it must also

269   be taken into account that the laser output needs to be modified depending on the

270   wavelength of the incident laser and the matrix studied.

271   Tables 2 and 3 show Raman peaks and the different iron corrosion products

272   formed in each cementitious matrix with different laser powers using wavelengths of

273   532 and 633 nm. According to Chitty et al. [31] the corrosion system was made up of a

274   multilayer structure constituted of a metallic substrate (M), a dense corrosion product

275   layer (DPL), a transformed medium (TM) and a binder (B). In the light of Raman

276   results presented in this paper, different iron compounds and heterogeneous dense

277   corrosion product layers (DPL) were observed on the steel extracted from alkali

278   activated fly ash mortars. The type of iron phases formed was dependent on the type of

279   alkaline solution used in the activation of fly ash and the amount of chloride added to

280   the cementitious system, while the heterogeneous DPL was associate with the detection

281   of two regions: dark and light. The difference in the colour of the rusts was associated

282   with different thickness in the dense product layer. Previous authors also considered that

283   the DPL thicknesses increased with the age of the sample, however in our case

284   thickness depend on the aggressive solution. A higher thickness of DPL and detection

285   of more crystalline compounds were observed in the dark areas. The corrosion products

286   in the light regions were poor crystallized phases of iron oxyhydroxide while the

287   products in the dark regions were goethite, except for FAB mortar in the presence of

288   0.4% Cl^- where lepidocrocite was formed. These results are in good agreement with

289   precedent data published on dense corrosion product layer of steel embedded in

290   concrete [5, 32]. However, neither Fe_3O_4, FeO nor akaganeite were detected in these

291   corrosion layers, no formation of the latter compound indicated that the amount of

292   chlorine was not enough in the DPL to stabilise this phase. Additionally Hostis et al.

293   [33] only found FeO, Fe_3O_4 as a tinny layer before embedded in concrete and the

294   corrosion phases formed were mainly iron oxyhydroxides (goethite).

295   Regarding the influence of the studied matrix (the type of alkaline solution used

296   in the activation of fly ash), it should be remembered that the FA was activated with two

297   alkaline solutions, one constituted only by NaOH (to manufacture FAA mortars) and

298   other consisting of a mixture of NaOH and waterglass (to manufacture the FAB

299   mortars). The matrix obtained with the solution containing a small amount of waterglass

300 (15%) was denser and more compact, and therefore chloride ion mobility to the steel

301 surface was more hindered and the corrosion process was more restricted [34]. The iron

302 corrosion products formed on the steel surface embedded in the FAB mortars were iron

303 oxyhydroxides with low crystallinity, lepidocrocite and goethite, while poor crystallized

304 phases of iron oxyhydroxides and goethite were detected in those formed on the FAA

305 mortars. In addition, the aggressivity of the medium (the amount of chloride added to

306 the cementitious system: 0.4 and 2% chlorides) also affected the nature of the corrosion

307 products. In the FAB mortar with 0.4% chlorides (FAB0.4) with a dense matrix and

308 lower amount of chlorides, slightly aggressive medium, lepidocrocite was formed.

309   The goethite present in the DPL is considered electrochemically stable. In

310 contrast, lepidocrocite plays an active role in the corrosion mechanisms [35]. The

311 dissolution of this phase in the wet stages is facilitated by slightly acidic media, leading

312 to the dissolution of lepidocrocite and the precipitation of amorphous ferric

313 oxyhydroxide upon drying. Finally, the amorphous ferric oxyhydroxide is transformed

314 to goethite [36]. As such, the FAB mortar with 0.4% chlorides may be an insufficiently

315 aggressive medium to promote the evolution of the rust in just 720 days, compared to

316 the rest of the mortars, where the evolution of lepidocrocite to goethite has indeed taken

317 place. Therefore, the characteristics of the cementitious matrices and the percentage of

318 chloride ions influenced the nature of the iron phases.

319   Turning our attention to the influence of the incident laser wavelength on the

320 iron corrosion products, the main objective of this work, well resolved Raman spectra

321 could be obtained with laser powers between 0.025 and 0.25 mW for a wavelength of

322 532 nm (more energy) and with laser powers of 0.25 to 2.5 mW for a wavelength of 633

323 nm.

324   No peak or only small peaks were detected in Raman spectra obtained for the

325   samples with both lasers at low power, 0.0005 mW with the 532 nm line and 0.25 mW

326   with the 633 nm line. The attribution of these peaks was complicated.

327   The most important difference between the two wavelengths was associated with

328   the stability of the iron corrosion products under laser heat during the tests. The phases

329   formed: iron oxyhydroxides, goethite or lepidocrocite, were transformed into hematite

330   or modified hematite at power equal to or above 0.5 mW using the laser line of 532 nm.

331   For the laser with the high wavelength of 633 nm, the phases remained stable for all the

332   conditions. Moreover, Raman spectra for the steel embedded in the four mortars

333   obtained with the laser line 532 nm and high power (5 mW) showed fluorescence,

334   leading to an increase in Raman intensity and a loss of peak definition of the corrosion

335   products.

Conclusions

337   The main corrosion products generated on the surface of steel embedded in

338   activated fly ash mortars in the presence of chlorides were poorly crystallised phases of

339   iron oxyhydroxides, goethite (α-FeOOH) and lepidocrocite (γ-FeOOH).

340   The iron products formed should be studied with a laser line of 532 nm and a

341   power from 0.025 to 0.25 mW or with a laser line of 633 nm and a power greater than

342   2.5 mW. The spectra obtained with the 532 nm line and 0.0005 mW or with the 633 nm

343   line and 0.25 mW presented low resolution, no peak or only small peaks were detected.

344   For the wavelength of 532 nm the phases formed: oxyhydroxides with low

345   crystallinity, goethite and lepidocrocite, were transformed into hematite or modified

346   hematite at a power equal to or above 0.5 mW. The spectra recorded with this line with

347   5 mW showed fluorescence.

Acknowledgements

354 **References**

355 1. Zitrou E, Nikolaou J, Tsakiridis PE, Papadimitriou GD. Atmospheric corrosion

356   of steel reinforcing bars produced by various manufacturing processes. Constr

357   Build Mater 2007;21:1161−9.

358 2. Almusallam AA. Effect of degree of corrosion on the properties of reinforcing

359   steel bars. Constr Build Mater 2001;15:361−8.

360 3. González JA, Miranda J. Corrosión en las Estructuras de Hormigón Armado:

361   Fundamentos, Medida, Diagnosis y Prevención. Consejo Superior de

362   Investigaciones Científicas, 30, Madrid:Biblioteca de Ciencias; 2007.

363 4. Poupard O, L'Hostis V, Catinaud S, Petre-Lazar I. Corrosion damage diagnosis

364   of a reinforced concrete beam after 40 years natural exposure in marine

365   environment. Cement Concrete Res 2006;36:504−20.

366 5. L'Hostis V, Neff D, Bellot-Gurlet L, Dillmann P. Characterization of long-term

367   corrosion of rebars embedded in concretes sampled on French historical

368   buildings aged from 50 to 80 years. Mater Corros 2009;60:93−8.

369 6. Ahmad S. Reinforcement corrosion in concrete structures, its monitoring and

370   service life prediction—a review. Cement Concrete Comp 2003;25:459−71.

371 7. Criado M, Martínez-Ramirez S, Fajardo S, Gómez PP, Bastidas JM. Corrosion

372   rate and corrosion product characterisation using Raman spectroscopy for steel

373   embedded in chloride polluted fly ash mortar. Mater Corros 2013;64:372−80.

8. Ghods P, Isgor OB, Burkan O, Bensebaa F, Kingston D. Angle-resolved XPS study of carbon steel passivity and chloride-induced depassivation in simulated concrete pore solution. Corros Sci 2012;58:159−67.

9. Aperador W, Mejía de Gutiérrez R, Bastidas DM. Steel corrosion behaviour in carbonated alkali-activated slag concrete. Corros Sci 2009;51:2027−33.

10. Mohammadi F, Nickchi T, Attar MM, Alfantazi A. EIS study of potentiostatically formed passive film on 304 stainless steel. Electrochim Acta 2011;56:8727−33.

11. Fajardo S, Bastidas DM, Ryan MP, Criado M, McPhail DS, Bastidas JM. Low-nickel stainless steel passive film in simulated concrete pore solution: A SIMS study. Appl Surf Sci 2010;256:6139−43.

12. Souier T, Martin F, Bataillon C, Cousty J. Local electrical characteristics of passive films formed on stainless steel surfaces by current sensing atomic force microscopy. Appl Surf Sci 2010;256:2434−9.

13. Larroumet D, Greenfield D, Akid R, Yarwood J. Raman spectroscopic studies of the corrosion of model iron electrodes in sodium chloride solution. J Raman Spectrosc 2007;38:1577−85.

14. Chen W, Du R-G, Ye C-Q, Zhu Y-F, Lin C-J. Study on the corrosion behavior of reinforcing steel in simulated concrete pore solutions using in situ Raman spectroscopy assisted by electrochemical techniques. Electrochim Acta 2010;55:5677−82.

15. Dubois F, Mendibide C, Pagnier T, Perrard F, Duret C. Raman mapping of corrosion products formed onto spring steels during salt spray experiments. A correlation between the scale composition and the corrosion resistance. Corros Sci 2008;50:3401−9.

399   16. Baek W-C, Kang T, Sohn H-J, Kho YT. In situ surface enhanced Raman

400   spectroscopic study on the effect of dissolved oxygen on the corrosion film on

401   low carbon steel in 0.01 M NaCl solution. Electrochim Acta 2001;46:2321−5.

402   17. Neff D, Bellot-Gurlet L, Dillmann P, Reguer S, Legrand L. Raman imaging of

403   ancient rust scales on archaeological iron artefacts for long-term atmospheric

404   corrosion mechanisms study. J Raman Spectrosc 2006;37:1228−37.

405   18. L'Hostis V, Amblard E, Guillot W, Paris C, Bellot-Gurlet L. Characterisation of

406   the steel concrete interface submitted to chloride-induced-corrosion. Mater

407   Corros 2013;64:185−94.

408   19. Colomban P, Cherifi S, Despert G. Raman identification of corrosion products on

409   automotive galvanized steel sheet. J Raman Spectrosc 2008;39:881−6.

410   20. de Faria DLA, Venancio-Silva S, de Oliveira MT. Raman microspectroscopy of

411   some iron oxides and oxyhydroxides. J Raman Spectrosc 1997;28:873−8.

412   21. Nieuwoudt MK, Comins JD, Cukrowski I. The growth of the passive film on iron

413   in 0.05 M NaOH studied in situ by Raman micro-spectroscopy and

414   electrochemical polarisation. Part I: near-resonance enhancement of the Raman

415   spectra of iron oxide and oxyhydroxide compounds. J Raman Spectrosc

416   2011;42:1335−9.

417   22. Bernal SA, Provis JL. Durability of Alkali-Activated Materials: Progress and

418   Perspectives. J Am Ceram Soc 2014;97:997−1008.

419   23. UNE 80−225−93 Spanish Standard, Test method for cements: chemical analysis.

420   Determination of the reactive silica (SiO_2) content in cements, pozzolans and fly

421   ashes;1993.

24. Arjuman P, Silbee MR, Roy DM. Quantitative determination of the crystalline and amorphous phases in low calcium fly ash. Ed. H. Justnes, In: Proc. 10thICCC Gothenburg, Sweden; 1997:3v 020 4.

25. Criado M, García-Díaz I, Bastidas JM, Alguacil FJ, López FA, Monticelli C. Effect of recycled glass fiber on the corrosion behavior of reinforced mortar. Constr Build Mater 2014;64:261–9.

26. Nauer G, Strecha P, Brinda-Konopikand N, Liptay G. Spectroscopic and thermoanalytical characterization of standard substances for the identification of reaction products on iron electrodes. J Therm Anal 1985;30:813–30.

27. Froment F, Tournié A, Colomban P. Raman identification of natural red to yellow pigments: ochre and iron-containing ores. J Raman Spectrosc 2008;39:560–8.

28. Bouchar M, Foy E, Neff D, Dillman P. The complex corrosion system of a medieval iron rebar from the Bourges. Corros Sci 2013;76:361–72.

29. Singh JK, Singh DDN. The nature of rusts and corrosion characteristics of low alloy and plain carbon steels in three kinds of concrete pore solution with salinity and different pH. Corros Sci 2012;56:129–42.

30. El Mendili Y, Bardeau J-F, Randrianantoandro N, Grasset F, Greneche J-M. Insights into the mechanism related to the phase transition from γ-Fe2O3 to α-Fe2O3 nanoparticles induced by thermal treatment and laser irradiation. J Phys Chem C 2012;116:23785-23792.

31. Chitty W-J, Dillmann P, L'Hostis V, Lombard C. Long-term corrosion resistance of metallic reinforcements in concrete—a study of corrosion mechanisms based on archaeological artefacts. Corros Sci 2005;47:1555–81.

446 32. Duffó GS, Reinoso M, Ramos CP, Farina SB. Characterization of steel rebars

447   embedded in a 70-year old concrete structure. Cement Concrete Res

448   2012;42:111–7.

449 33. L'Hostis V, Foct F, Dillmann P. Corrosion behaviour of reinforced concrete:

450   Laboratory experiments and archaeological analogues for long-term predictive

451   modelling. J Nucl Mater 2008;379:124–32.

452 34. Criado M, Bastidas DM, Fajardo S, Fernández-Jiménez A, Bastidas JM.

453   Corrosion behaviour of a new low-nickel stainless steel embedded in activated

454   fly ash mortars. Cement Concrete Comp 2011;33:644–52.

455 35. Monnier J, Bellot-Gurlet L, Baron D, Neff D, Guillot I, Dillmann P. A

456   methodology for Raman structural quantification imaging and its application to

457   iron indoor atmospheric corrosion products. J Raman Spectrosc

458   2011;42:773–781.

459 36. Misawa T, Asami K, Hashimoto K, Shimodaira S. The mechanism of

460   atmospheric rusting and the protective amorphous rust on low alloy steel. Corr.
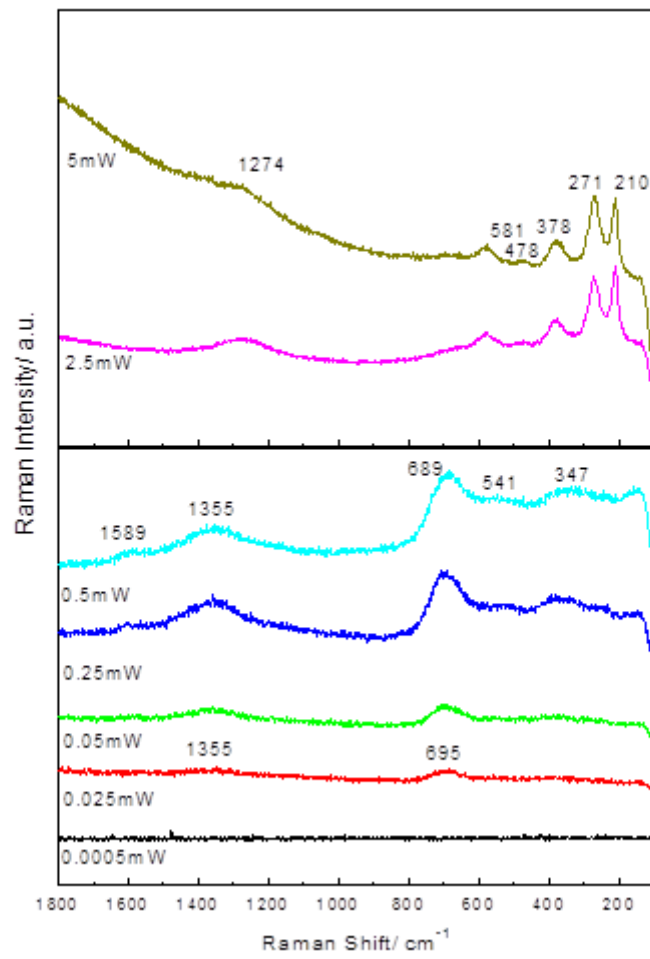
461   Sci. 1974;14:279-89.

462

463

464 **FIGURES**
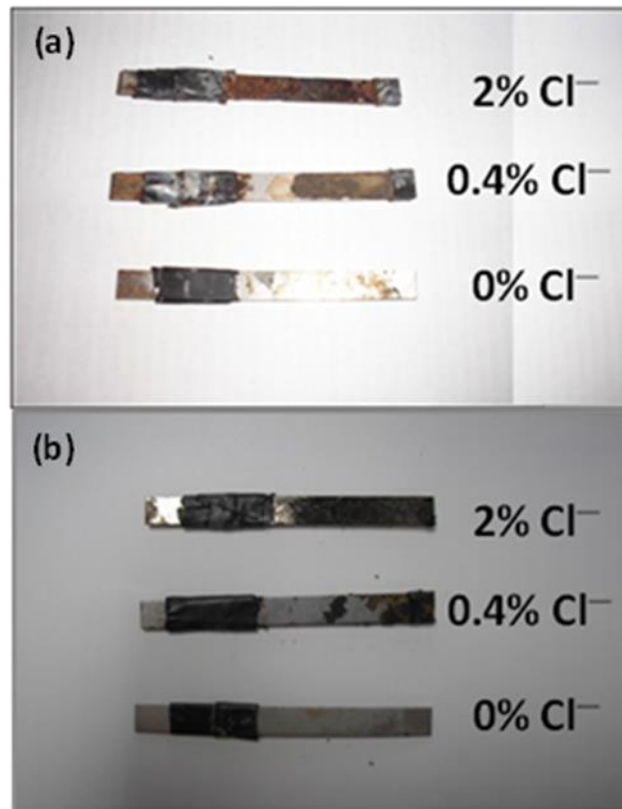
465

466 Fig. 1. Steel specimens extracted from the (a) FAA and (b) FAB mortars without

467 chlorides and with 0.4 and 2% chlorides after 720 days of experimentation.
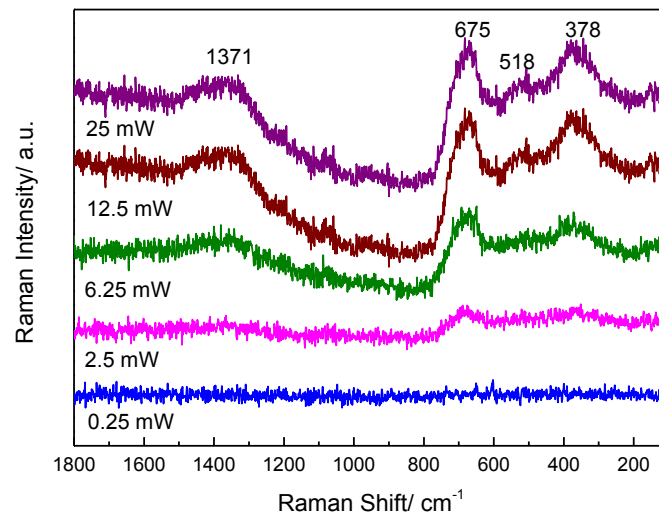
468

469

470 Fig. 2. In situ Raman spectra of the corroded bar embedded in FAA mortar with 0.4%

471 chlorides using an optimised excitation wavelength of 532 nm under different laser
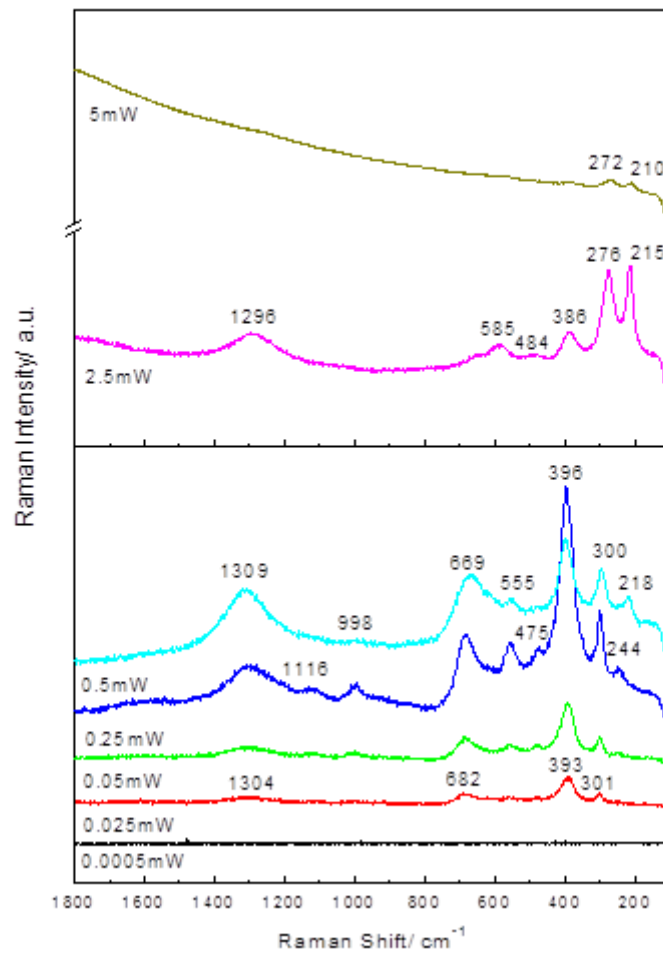
472 output power.

473

474

475   Fig. 3. In situ Raman spectra of the corroded bar embedded in FAA mortar with 0.4%

476   chlorides using an optimised excitation wavelength of 633 nm under different laser

477   output power.

478

479

480

481   Fig. 4. In situ Raman spectra of the corroded bar embedded in FAA mortar with 2%

482   chlorides using an optimised excitation wavelength of 532 nm under different laser
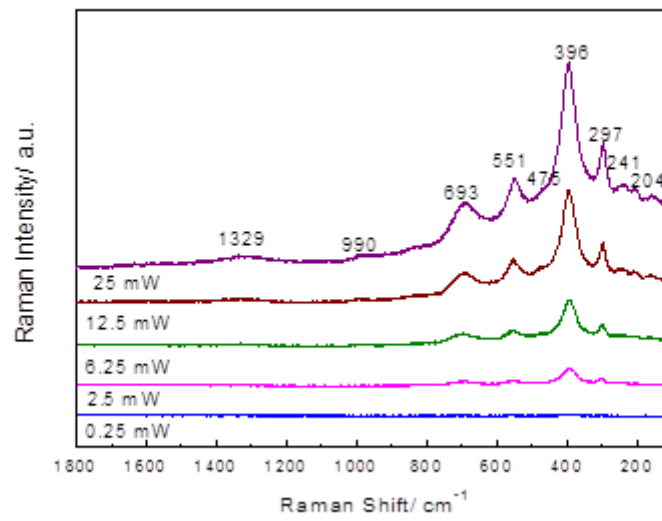
483   output power.

484

485

486

487

488

489

490

491

Fig. 5. In situ Raman spectra of the corroded bar embedded in FAA mortar with 2% chlorides using an optimised excitation wavelength of 633 nm under different laser output power.
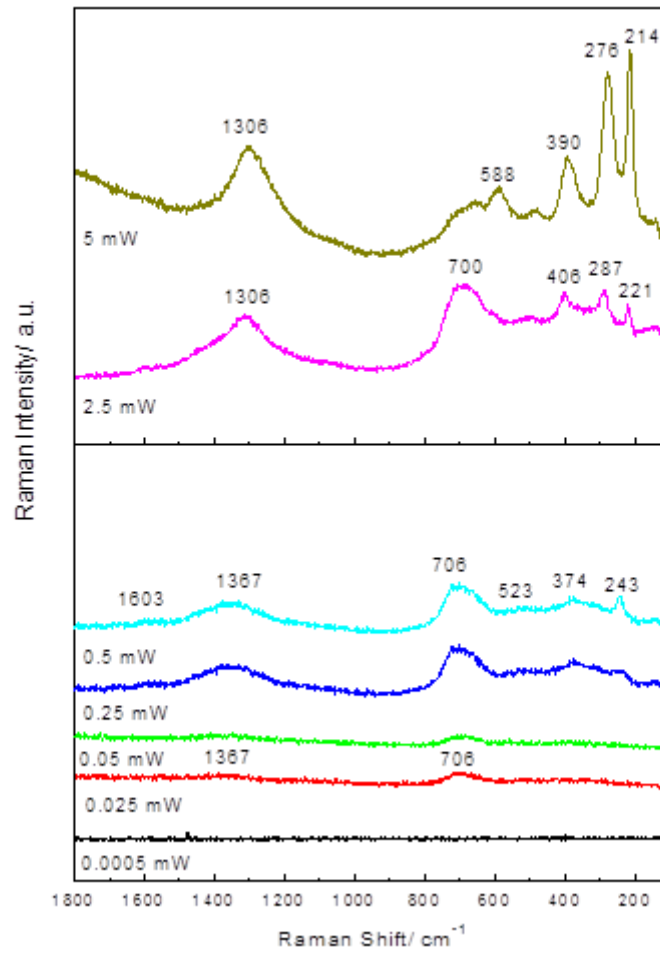
510

511

512 Fig. 6. In situ Raman spectra of the corroded bar embedded in FAB mortar with 0.4%

513 chlorides using an optimised excitation wavelength of 532 nm under different laser
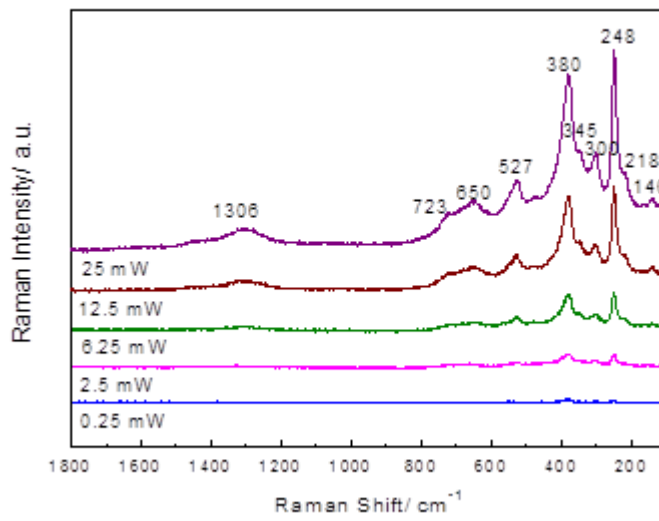
514 output power.

515

516

517

518

519

520

Fig. 7. In situ Raman spectra of the corroded bar embedded in FAB mortar with 0.4% chlorides using an optimised excitation wavelength of 633 nm under different laser output power.

538

539   Fig. 8. In situ Raman spectra of the corroded bar embedded in FAB mortar with 2%

540   chlorides using an optimised excitation wavelength of 532 nm under different laser

541   output power.

542
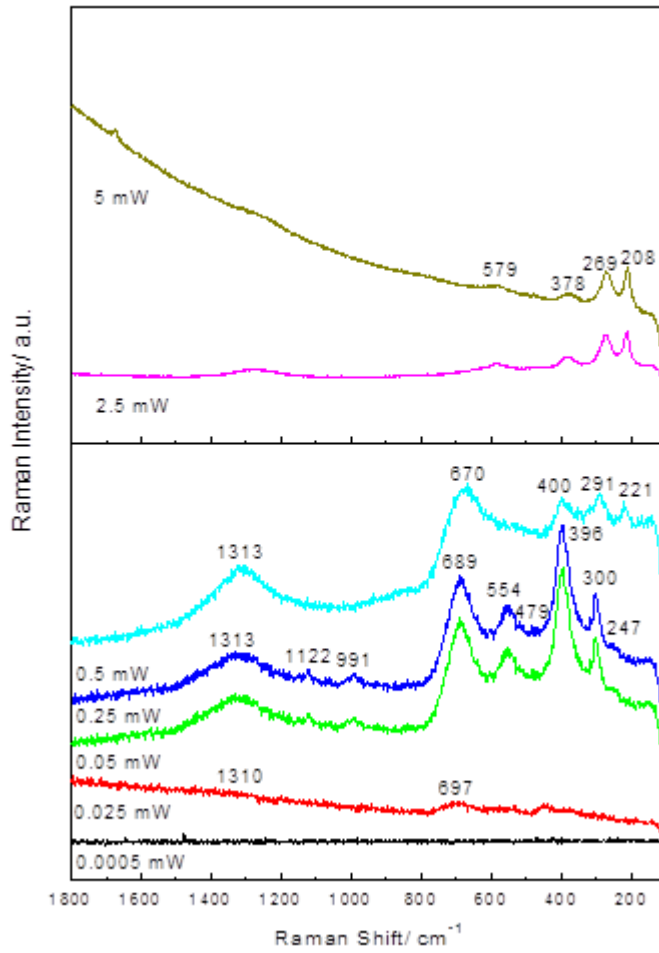
543

544

545

546

547

548

549
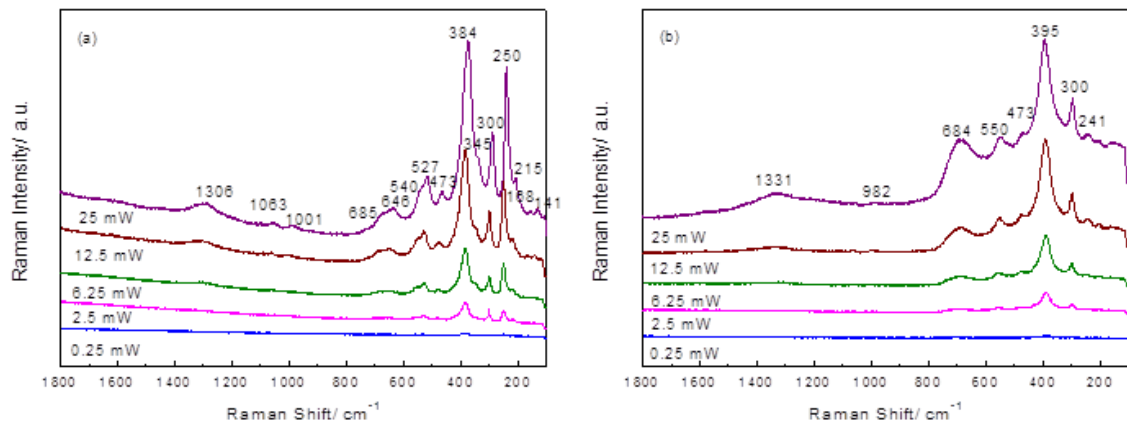
Fig. 9. In situ Raman spectra of the corroded bar embedded in FAB mortar with 2% chlorides using an optimised excitation wavelength of 633 nm under different laser output power, (a) light and (b) dark regions.

557

558   Table 1. Chemical composition of the tested fly ash (% mass).

559

SiO$_2$	Al$_2$O$_3$	Fe$_2$O$_3$	CaO	MgO	SO$_3$	Na$_2$O	K$_2$O	MnO	P$_2$O$_5$	TiO$_2$	LOI	Others	Total
51.78	27.80	6.18	4.59	1.52	0.71	0.59	2.51	0.06	0.62	1.35	2.23	0.06	100

560   LOI: Loss on ignition
561
562

563 Table 2. Raman peaks and main phases identified in FAA mortar with the different

564 powers for the wavelengths of 532 and 633 nm.

Frequency (cm^{-1})	FAA mortar						
	λ = 633 nm		λ = 532 nm				
	0.4%	2%	0.4%		2%		
	0.25mW-25mW	0.25mW-25mW	0.05mW-0.5mW	2.5mW-5mW	0.025mw-0.05mW	0.25mW-0.5mW	2.5mW-5mW
693		m,b	b				
684					w,b		
675	b						
669						m,b	
650							
581				m	m,b		m
550		m				m,b	
540			w, b				
527	b						
518							
475		sh	w			w	w
396		s			s	s	m,b
380	b			m			
345			w,b				
300		m			m	s	
272				s			s
244						m	
215				s		m	s
Identified phases	O; G [13,17,18, 21, 27]	O; G [13,17,18, 21, 27]	O; G [13,17,18, 21, 27]	M.H.	G [13,18, 21, 27]	G; M.H [13,18, 21, 27]	M.H

565 s: strong; m: medium; b: broad; w: weak; sh: sharp

566 O: iron oxyhydroxides with low crystallinity; G = Goethite; M.H. Modified Hematite;

567

568 Table 3. Raman peaks and main phases identified in FAB mortar with the different

569 powers for the wavelengths of 532 and 633 nm.

Frequency (cm^{-1})	FAB mortar									
	λ = 633 nm			λ = 532 nm						
	0.4%	2%		0.4%			2%			
		0.25mW-25mW		0.025mW-0.5mW	2.5mW	5mW	0.025mW	0.05mW-0.25mW	0.5mW	2.5mW-5mW
	0.25mW-25mW	Dark region	Light region							
706				m,b	s,b	m,b				
693							b	m		
684		m,b	m,b							
675	m								m	
650			m,b							
588						m,b				
579										m,b
559								m		
550		m								
540	m		m							
527			m							
518										
475		sh	w				b			
396		s			m	m		s	m	
380	s		s							m,b
374				w						
345	sh		sh							
300		s	s					s		
287					m				m	
270						s				s
248		w	s	w						
221					m				m	
214						s				s
Identified phases	L [13,17,18]	G; L [13,17,18,21,27]	G; L [13,17,18,21,27]	O; L [13,17,18,21,27]	H [19]	M.H	O [17,18]	G [13,17,18,21,27]	H [19]	M.H

570 s: strong; m: medium; b: broad; w: weak; sh: sharp
571 L: Lepidocrocite; O: iron oxyhydroxides with low crystallinity; G = Goethite; M.H.
572 Modified Hematite
573